

Influence of the nanofiber chemistry and orientation of biodegradable poly(butylene succinate)-based scaffolds on osteoblast differentiation for bone tissue regeneration

Citation for published version (APA):

Cristofaro, F., Gigli, M., Bloise, N., Chen, H., Bruni, G., Munari, A., Moroni, L., Lotti, N., & Visai, L. (2018). Influence of the nanofiber chemistry and orientation of biodegradable poly(butylene succinate)-based scaffolds on osteoblast differentiation for bone tissue regeneration. *Nanoscale*, 10(18), 8689-8703. <https://doi.org/10.1039/c8nr00677f>

Document status and date:

Published: 14/05/2018

DOI:

[10.1039/c8nr00677f](https://doi.org/10.1039/c8nr00677f)

Document Version:

Publisher's PDF, also known as Version of record

Document license:

Taverne

Please check the document version of this publication:

- A submitted manuscript is the version of the article upon submission and before peer-review. There can be important differences between the submitted version and the official published version of record. People interested in the research are advised to contact the author for the final version of the publication, or visit the DOI to the publisher's website.
- The final author version and the galley proof are versions of the publication after peer review.
- The final published version features the final layout of the paper including the volume, issue and page numbers.

[Link to publication](#)

General rights

Copyright and moral rights for the publications made accessible in the public portal are retained by the authors and/or other copyright owners and it is a condition of accessing publications that users recognise and abide by the legal requirements associated with these rights.

- Users may download and print one copy of any publication from the public portal for the purpose of private study or research.
- You may not further distribute the material or use it for any profit-making activity or commercial gain
- You may freely distribute the URL identifying the publication in the public portal.

If the publication is distributed under the terms of Article 25fa of the Dutch Copyright Act, indicated by the "Taverne" license above, please follow below link for the End User Agreement:

www.umlib.nl/taverne-license

Take down policy

If you believe that this document breaches copyright please contact us at:

repository@maastrichtuniversity.nl

providing details and we will investigate your claim.

Download date: 17 Apr. 2024



Cite this: *Nanoscale*, 2018, **10**, 8689

Influence of the nanofiber chemistry and orientation of biodegradable poly(butylene succinate)-based scaffolds on osteoblast differentiation for bone tissue regeneration†

Francesco Cristofaro,  ‡^{a,b} Matteo Gigli,  ‡^c Nora Bloise,  ^{a,b} Honglin Chen,^d Giovanna Bruni,  ^e Andrea Munari,  ^f Lorenzo Moroni,  ^{d,g} Nadia Lotti  ^{*f} and Livia Visai  ^{*a,b}

Innovative nanofibrous scaffolds have attracted considerable attention in bone tissue engineering, due to their ability to mimic the hierarchical architecture of an extracellular matrix. Aiming at investigating how the polymer chemistry and fiber orientation of electrospun scaffolds (ES) based on poly(butylene succinate) (PBS) and poly(butylene succinate/diglycolate) (P(BS80BDG20)) affect human osteoblast differentiation, uniaxially aligned (a-) and randomly (r-) distributed nanofibers were produced. Although human osteoblastic SAOS-2 cells were shown to be viable and adherent onto all ES materials, a-P(BS80BDG20) exhibited the best performance both in terms of cellular phosphorylated focal adhesion kinase expression and in terms of alkaline phosphatase activity, calcified bone matrix deposition and quantitative gene expression of bone specific markers during differentiation. It has been hypothesized that the presence of ether linkages may lead to an increased density of hydrogen bond acceptors along the P(BS80BDG20) backbone, which, by interacting with cell membrane components, can in turn promote a better cell attachment on the copolymer mats with respect to the PBS homopolymer. Furthermore, although displaying the same chemical structure, r-P(BS80BDG20) scaffolds showed a reduced cell attachment and osteogenic differentiation in comparison with a-P(BS80BDG20), evidencing the importance of nanofiber alignment. Thus, the coupled action of polymer chemical structure and nanofiber alignment played a significant role in promoting the biological interaction.

Received 24th January 2018,

Accepted 29th March 2018

DOI: 10.1039/c8nr00677f

rscl.li/nanoscale

^aMolecular Medicine Department (DMM), Center for Health Technologies (CHT), UdR INSTM, University of Pavia, Via Taramelli 3/B, 27100 Pavia, Italy.

E-mail: livia.visai@unipv.it; Fax: +39 0382423108; Tel: +39 0382987725

^bDepartment of Occupational Medicine, Toxicology and Environmental Risks, Istituti Clinici Scientifici Maugeri S.p.A., IRCCS, Via S. Boezio, 28, 27100 Pavia, Italy

^cDepartment of Chemical Science and Technologies, University of Roma Tor Vergata, Via della Ricerca Scientifica 1, 00133 Roma, Italy

^dMERLN Institute for Technology Inspired Regenerative Medicine, Department of Complex Tissue Regeneration, Maastricht University, The Netherlands

^eDepartment of Chemistry, Section of Physical Chemistry, University of Pavia, Via Taramelli 12, 27100 Pavia, Italy

^fDepartment of Civil, Chemical, Environmental and Materials Engineering, University of Bologna, Via Terracini 28, 40131 Bologna, Italy.

E-mail: nadia.lotti@unibo.it; Fax: +39 0512090322; Tel: +39 0512090354

^gCNR NANOTEC Institute of Nanotechnology, c/o Campus Ecotekne, Università del Salento, Italy

†Electronic supplementary information (ESI) available. See DOI: 10.1039/c8nr00677f

‡Both authors contributed equally.

1. Introduction

Bone tissue is the major structural and supportive connective tissue of the body. It may be considered as a nanocomposite consisting of organic (mostly collagen and other small bone-related proteins) and inorganic matrixes composed of hydroxyapatite (HA) containing calcium phosphate.¹ Typical bone cells comprise osteoblasts, bone lining cells, osteocytes, and osteoclasts, which are embedded in the bone extracellular matrix (ECM). Osteoblasts are responsible for the synthesis of the organic ECM and modification of matrix mineralization; osteocytes are involved in mineral homeostasis, whereas osteoclasts can resorb bone and play significant roles in cell growth and bone regeneration. The loss or dysfunction of bone tissue that can accompany trauma, injury, disease or advancing years can result in significant morbidity as well as in a variety of socio-economic issues. Worldwide incidence of bone disorders is expected to double in 2020, due to population aging and increased life expectancy. That is why, currently, the reconstruction of a damaged bone tissue remains very challenging.

Aiming to develop new therapeutic products that utilize a combination of scaffolds with viable cell systems or their derived responsive biomolecules for the repair and restoration/regeneration of tissues, tissue engineering and regenerative medicine can play an important role in this respect. In recent years, the advent of nanotechnology in bone regenerative medicine has transfigured the designing of grafts and scaffolds, allowing for the development of new grafts and scaffold systems (which include nanoparticles, nanofibers and nanocomposites) that show significantly enhanced cellular and tissue regenerative properties.^{2,3} The latest advances in the development of scaffolds using nanotechnology have given the surgeon new options for restoring the form and function of tissues and organs.^{4,5} One of the most pivotal elements in bone tissue regeneration consists in creating and developing scaffolds, such as a biodegradable highly porous microstructure with interrelated pores and a large surface area, capable of mimicking the ECM microstructure, thus providing mechanical properties to support bone ingrowth.⁴⁻⁷ In this context, electrospinning, a versatile and advanced technique for the production and fabrication of complex nanofibrous assemblies, attracted remarkable attention, essentially due to two different factors: (i) the capacity of structural mimicking of the natural tissues of ECM, and (ii) the possibility to process a wide range of materials together with a simple set-up and cost-effectiveness.⁴⁻⁹ In particular, nanosurface modification by the electrospinning technique is able to control the protein adsorption and the biochemical construction of the protein layer. Constructing 'bottom up' nanoscale features can ultimately direct the surface hydrophilicity, the oxide thickness or the distribution of functional groups. Surface topography can also direct protein orientation and denaturation, which downstream obviously controls cell surface proliferation. A wide range of natural and synthetic biodegradable polymers, such as alginate, chitosan, collagen, poly-caprolactone (PCL), poly-glycolic acid (PGA), poly-lactic acid (PLA) and poly(lactic-co-glycolic acid) (PLGA), and blended polymers, have been employed in the production of electrospun nanofibrous scaffolds for bone regeneration.⁴⁻⁶ Furthermore, osteogenic agents, nanostructured materials or inorganic phase materials, like hydroxyapatite (HA) or β -tricalcium phosphate (β -TCP), which is one of the compositions of natural bone or bone precursors, have been used to functionalize electrospun scaffolds in order to improve the biomaterials' structure, mechanical properties, cellular adhesion and osteogenic differentiation.⁴⁻⁷

More recently, other polyesters, such as poly(butylene succinate) (PBS), have been proposed for tissue engineering applications. The success of PBS is mainly due to its proven biodegradability and biocompatibility, as well as to its low cost and intriguing physical/mechanical properties.¹⁰ Moreover, the possibility of modifying and tailoring its properties, *e.g.* through copolymerization or blending, has provided researchers with a versatile material, capable of satisfying the requirements for a wide variety of applications, ranging from soft tissue engineering^{11,12} to cartilage¹³ and bone regeneration.¹⁴⁻¹⁶ In particular, in a previous work, electrospun scaffolds fabricated from a class of block PBS-based copolyesters containing either butylene thio-

diglycolate or butylene diglycolate sequences were tested for skeletal differentiation of human mesenchymal stromal cells.¹⁷ The electrospun scaffolds displayed tunable mechanical properties and hydrolysis rate depending on the molecular architecture and on the kind of heteroatom introduced along the polymer backbone. Furthermore, the *in vitro* biological investigations demonstrated better suitability of the ether-containing copolyesters for the regeneration of skeletal tissues.¹⁷ These results were the starting point of the current study. Since the biocompatibility outputs had been very promising, we decided to further investigate the response of these PBS-based polymers by employing osteoblastic cells. Indeed, in the abovementioned paper we found that "PBS-based copolyesters containing thioether linkages were more favourable for chondrogenesis of hMSCs, while, PBS-based copolyesters containing ether linkages showed enhanced mineralization".¹⁷ In view of the potential clinical applications, in the present work we focused on nanoelectrospun PBS-based copolymers containing ether linkages, *i.e.* poly(butylene succinate/diglycolate), for their promising use as implant coating biomaterials. In bone tissue engineering, biopolymers used for nanosurface modification have drawn great attention in order to improve osteointegration and implant fixation and reduce implant failure. Furthermore, from the literature analysis it emerged that, to the best of our knowledge, this is the first time that SAOS-2 cells have been used to evaluate the osteogenic differentiation of nanoelectrospun PBS and PBS-based polymers and composites for bone tissue regeneration.

In this framework, the goal of the present study was to investigate how polymer chemistry, *i.e.* the addition of ether linkages into the PBS backbone, and fiber orientation can affect osteoblast attachment and differentiation for promoting healing and bone formation processes. This approach is expected to impact both on material properties and on scaffold-cell interaction, due to a higher number of functional groups along copolymer macromolecular chains, which are capable of favouring fiber alignment as well as serving as anchoring points for cell attachment (as depicted in the cartoon in Fig. 1).

In particular, to evaluate their suitability for bone tissue regeneration, (i) aligned and random electrospun scaffolds of PBS and (P(BS80BDG20)) were fabricated, (ii) their physical/chemical properties and hydrolytic degradation profiles were presented, (iii) their biocompatibility was tested in terms of cell viability, morphology, FAK focal adhesion, and the growth of human osteoblastic SAOS-2, and (iv) SAOS-2 cell differentiation was investigated in terms of alkaline phosphatase (ALP) activity, calcified bone matrix deposition, and quantitative gene expression of bone specific markers.

2. Results and discussion

2.1. Characterization of electrospun fibres

The morphology of the obtained fibers was investigated by SEM (Fig. 2). The fiber orientation was determined by measuring the SEM image coherence. The analysis revealed that the

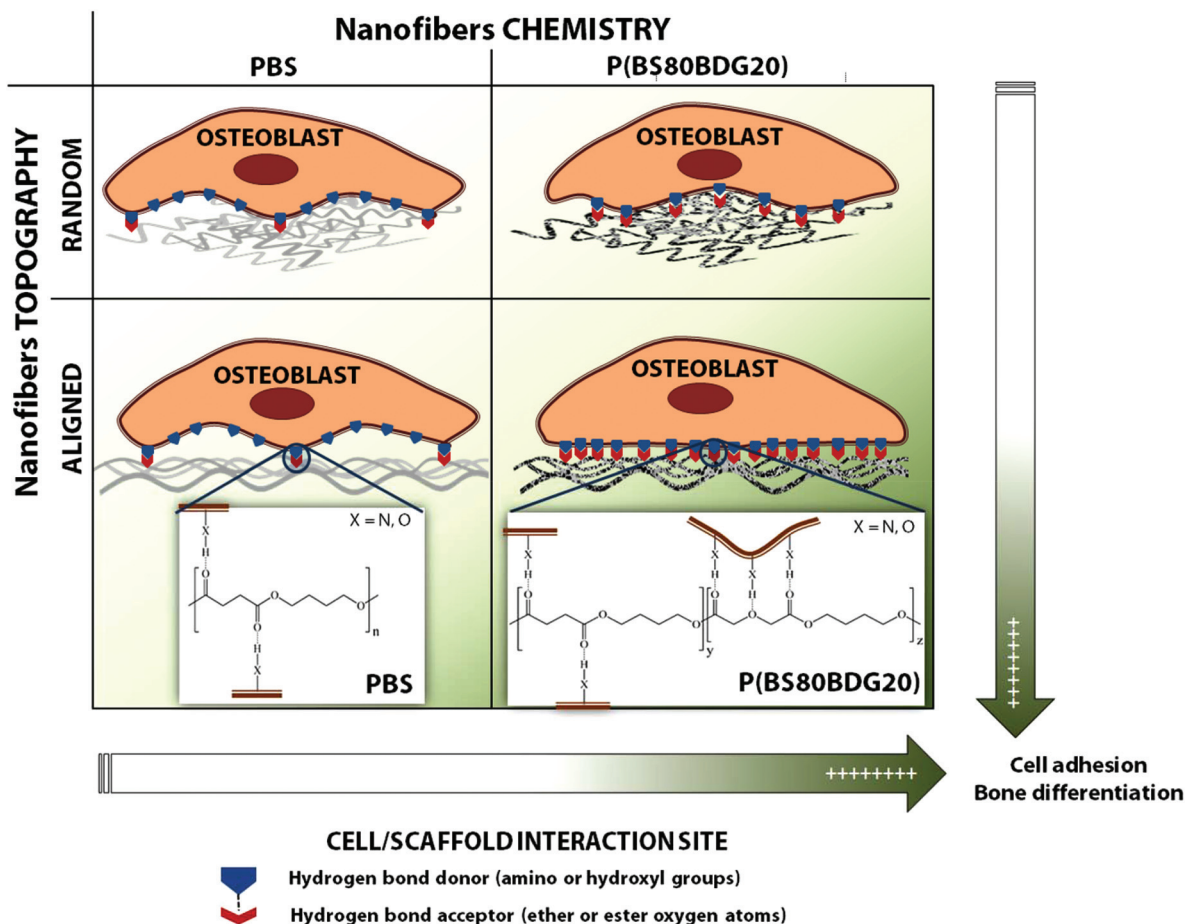


Fig. 1 Cartoon of the chemical structures of the two polymers under study and their conceivable chemical interactions with biological components.

coherence measurement of both aligned PBS (a-PBS) and P(BS80BDG20) (a-P(BS80BDG20)) was 0.66 and 0.77, respectively. In contrast, the values for both random PBS (r-PBS) and P(BS80BDG20) (r-P(BS80BDG20)) were 0.21 and 0.29, respectively. The fiber orientation was also confirmed by FFT images. Altogether, these results suggested that a-PBS and a-P(BS80BDG20) were successfully collected using a rotating mandrel. The higher alignment degree of P(BS80BDG20) fibers is most probably due to the higher interchain interactions generated by the presence of ether linkages along the copolymer backbone. In addition, fiber diameter distribution of the obtained fibers was calculated from SEM images (Fig. S1†). a-PBS and a-P(BS80BDG20) had an average fiber diameter of 270 ± 100 nm and 305 ± 136 nm, respectively. The average fiber diameter for r-PBS and r-P(BS80BDG20) was 254 ± 91 nm and 270 ± 102 nm, respectively. Thus, our results demonstrated that the obtained electrospun fibers had a comparable fiber size.

ES nanofibers of both PBS and P(BS80BDG20) were also characterized by GPC and TGA. Both techniques did not highlight any significant variation in molecular weight and thermal stability with respect to the polymer powders, confirming that the electrospinning process did not cause any degradation.

DSC measurements evidenced only negligible differences in the thermal behavior of electrospun fibers (Table 1) as compared to films.¹⁷ For both polymers, a glass transition and a melting endotherm were visible. P(BS80BDG20) displayed lower melting temperature and enthalpy of fusion (*i.e.* reduced degree of crystallinity) with respect to the parent homopolymer, due to the decrease of the block length of crystallizable BS segments. The degrees of crystallinity of the electrospun fibers, calculated using eqn (1) (Table 1), are in good agreement with those obtained by WAXS on polymeric films,¹⁸ indicating that the electrospinning treatment did not alter the crystallinity behavior of the samples.

Water contact angle measurements were performed to evaluate the surface wettability of PBS and P(BS80BDG20) mats. Performing these measurement on the scaffolds was not possible as the mats soaked up the water drops instantaneously, due to their high porosity. Therefore, WCA analyses were performed on the films. Results evidenced that the introduction of ether-oxygen containing co-units along the PBS macromolecular chain caused a slight increase of surface wettability (Table 1), because of the presence of highly electronegative oxygen atoms.

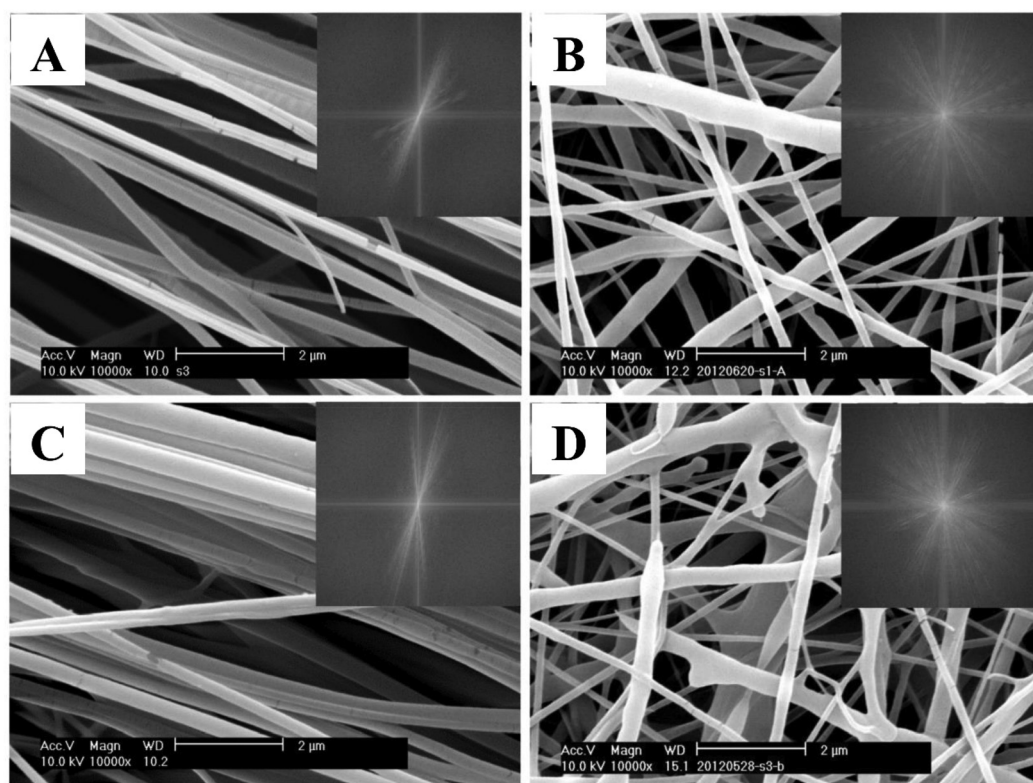


Fig. 2 SEM micrographs of electrospun fibers and FFT of SEM images (top right corner). (A) a-PBS, (B) r-PBS, (C) a-P(BS80BDG20), and (D) r-P(BS80BDG20).

Table 1 Molecular and thermal properties of PBS and P(BS80BDG20) scaffolds

Polymer	M_n	D	BDG (mol%)	$T_{5\% \text{ loss}}$ (°C)	T_{max} (°C)	T_g (°C)	ΔC_p (J °C ⁻¹ g ⁻¹)	T_m (°C)	ΔH_m (J g ⁻¹)	X_c (%)	WCA (°)
PBS	51 000	2.2	100	303	390	-36	0.101	115	81	41	96 ± 1
P(BS80BDG20)	54 000	2.0	81	318	395	-34	0.231	96	60	30	92 ± 2

2.2. Hydrolytic degradation

Hydrolytic degradation experiments were performed under physiological conditions on ES mats to evaluate their hydrolysis rate. Weight losses are reported in Fig. 3A as a function of incubation time.

After 203 days of incubation, PBS weight loss was almost negligible, while P(BS80BDG20) scaffolds degraded to a higher extent, reaching weight losses of about 7%. The copolymerization of PBS with BDG co-units enhanced its degradability, mainly because of a reduction of the degree of crystallinity and an increase of surface hydrophilicity, both well-known factors affecting the hydrolytic degradation rate of aliphatic polyesters.^{19,20} Partially degraded mats have also been subjected to molecular weight determination, since a significant decrease of molecular weight can be observed during the first stages of hydrolytic degradation, even if the weight losses are still negligible.²¹ The percentage of residual number average molecular weight ($M_{n \text{ res}}$ (%)) is shown in Fig. 3B as a function of incubation time. Both samples experienced a decrease of M_n with time, and the results supported the weight loss trend.

To confirm that the amorphous domains are more easily hydrolysed than the crystalline ones, partially degraded samples were analysed by DSC. All the calorimetric traces showed an endothermic peak associated with the melting of the polymer crystals. The corresponding heat of fusion was normalized with respect to the heat of fusion of the non-degraded sample ($\Delta H_f/\Delta H_0$). The results obtained are reported in Fig. 3C. It is worth noting that the increment of the crystalline/amorphous ratio can be also due to annealing, which occurs when a polymeric material is stored at a temperature between its T_g and T_m . Considering this, both samples have been incubated at 37 °C under a nitrogen atmosphere (to prevent any possible degradation process) and subjected to DSC measurements (Fig. 3C).

For PBS, the ΔH_m increase due to the annealing coincided with that observed for hydrolytically degraded samples. In contrast, in the case of P(BS80BDG20), the ΔH_m enhancement due to the annealing process was lower than that observed for the degraded samples, meaning that the ΔH_m increment is a combination of annealing and preferential degradation of the copolymer amorphous domains.

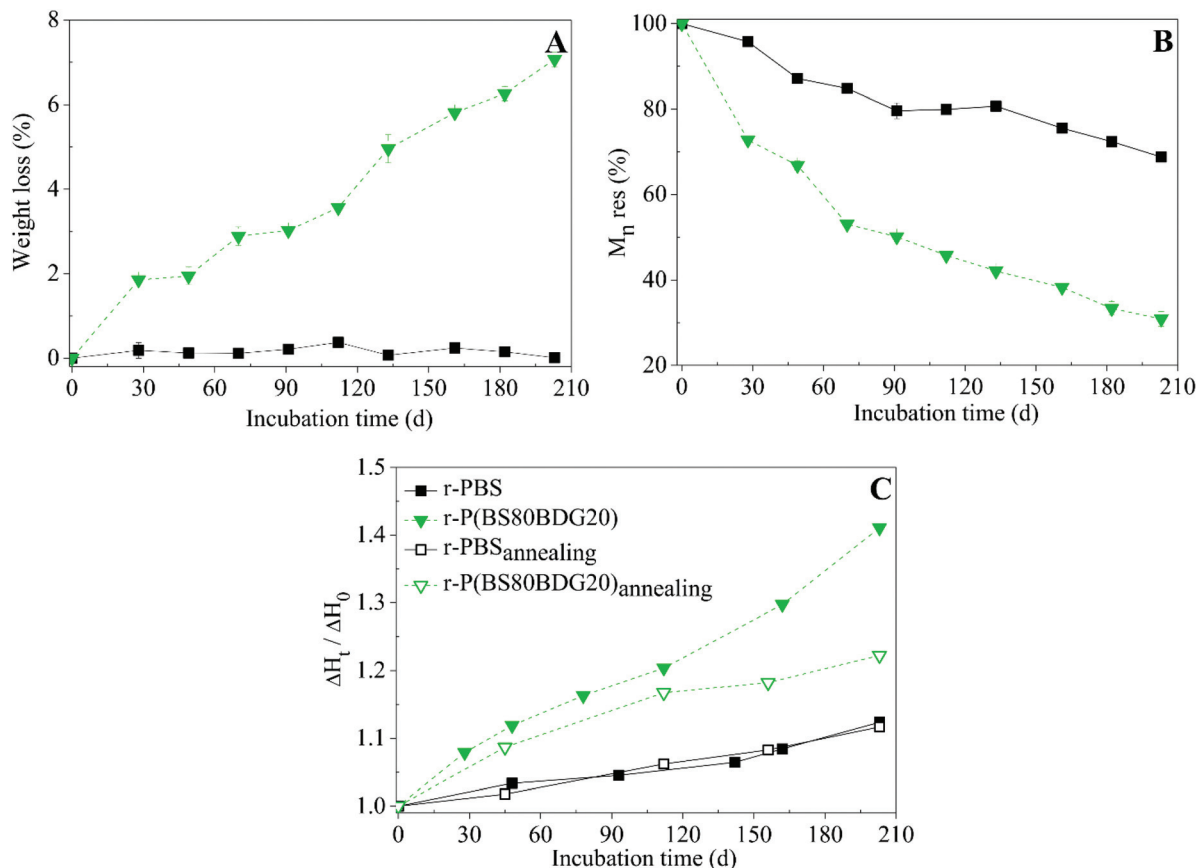


Fig. 3 Hydrolytic degradation studies of PBS and P(BS80BDG20) scaffolds as a function of incubation time. (A) Weight loss, (B) residual molecular weight, and (C) normalized heat of fusion.

2.3. Cell viability

The SAOS-2 cell line was selected because it exhibits several fundamental osteoblast characteristics²¹ and represents a widely used and well-accepted model for *in vitro* osteoblast study. These osteoblasts can virtually grow indefinitely and uniquely display osteoinductive activity.^{22–25} SAOS-2 viability, morphology and attachment at different times of incubation were properly analysed (Fig. 4 and 5). Osteoblast viability on a- and r-nanofibrous mats of both PBS and P(BS80BDG20) was expressed as percentage of the control (TCPS) (Fig. 4A). Cells displayed comparable viability at 1, 3 and 7 days, independently of the surface chemical composition (PBS or P(BS80BDG20)) or fiber orientation (aligned or random). In contrast, SAOS-2 viability was significantly ($p < 0.001$) reduced on both films of either PBS (f-PBS) or P(BS80BDG20) (f-P(BS80BDG20)) at each time point (Fig. 4A). Interestingly, cell viability was slightly higher on f-P(BS80BDG20) than on f-PBS.

Furthermore, to determine whether the interaction of SAOS-2 with films or a- and r-ES activated cell apoptosis, PSVue480™ reagent staining was performed after 24 h of cell seeding: no cell apoptosis was observed (data not shown).

To evaluate the effect of chemical composition and topography on cell morphology, SAOS-2 were observed using SEM

(Fig. 4B) and CLSM (Fig. 5A). Fig. 4B contains SEM micrographs of 1 and 7 d of cell culture on a- and r-nanofibrous mats as compared to Thermanox. Cells were more aligned and distributed along both a-PBS and a-P(BS80BDG20) with respect to r-PBS and r-P(BS80BDG20), the latter showing randomly dispersed cells (Fig. 4B and 5A). Furthermore, at higher magnification (insets of Fig. 4B), non-adhering SAOS-2 cells (round shape) were slightly more diffused on r-PBS, whereas on the other ES nanofibers a higher number of adherent cells with flattened shape homogeneously covered the surface. These results are consistent with the reported data on cell viability (Fig. 4A).

SAOS-2 cells have been also observed through immunofluorescence of F-actin and beta-tubulin filaments, as shown in Fig. 5A. No particular differences in morphology of adherent cells to both r-PBS and r-P(BS80BDG20) mats in comparison with the control (TCPS) were observed: SAOS-2 cells exhibited a mixed morphology of mainly round or elongated polygonal cells. F-Actin (in red) polymerized in a dense meshwork of quite well-defined stress fibers distributed throughout the body of cells seeded and cultured on TCPS, whereas that on r-electrospun fibers of both mats (Fig. 5A, insets of panels a, c and e) resulted more diffuse and less organized. The distribution pattern of beta-tubulin (green fluorescence) was similar

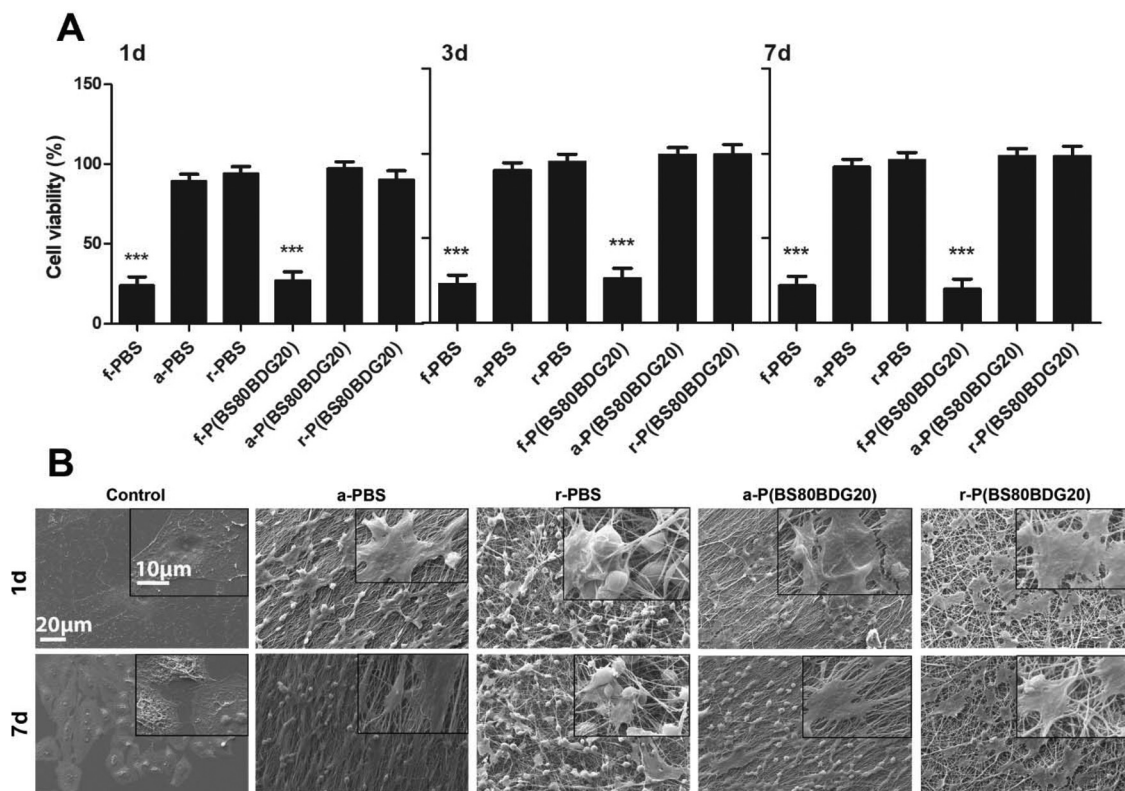


Fig. 4 SAOS-2 viability and morphology on electrospun nanofibers and flat films. (A) SAOS-2 viability on a- and r-electrospun nanofibers and on f-mats of both PBS and P(BS80BDG20) was evaluated at day 1, 3 and 7, respectively. Results are reported as percentage of cells related to those seeded on control (TCPS). Statistical significance values are indicated as *** $p < 0.001$. (B) Representative SEM images of SAOS-2 cultured on thermanox (as control) and on electrospun nanofibers of both PBS and P(BS80BDG20) at day 1 and 7 of culture. Scale bars represent 20 and 10 μm .

to F-actin (Fig. 5A, insets of panels a, c and e). For the control samples, microtubules were organized in a network originating in a perinuclear position that spread in a curved fashion throughout the body to its finest extensions. For both types of r-ES scaffolds a less organized cytoplasmic beta-tubulin distribution was observed (Fig. 5A, insets of panels a, c and e).

In contrast, the cytoskeleton of cells seeded on both a-PBS and a-P(BS80BDG20) showed some differences as compared to r-ES and control. The cells appeared more prolonged and positively distributed along the alignment of the nanofibers (Fig. 5A, panels b and d). This effect seems to be dependent more on the nanofiber alignment than on the chemical structure of the materials.

Interestingly, the beta-tubulin (in green) resulted more marked than F-actin (in red), suggesting the incomplete differentiation state of the cells on both a- and r-nanofibrous mats (Fig. 5A, panels b and d). Lastly, cell cytoskeleton morphology was not determined on films because very few cells were attached on either f-PBS or f-P(BS80BDG20): these data indirectly confirmed the lower cell viability (Fig. 4A), due to a lower cell attachment as compared to ES nanofibers. Cell attachment is a complex process affected by numerous aspects, such as cell behaviour and material surface properties, which include hydrophobicity, charge, roughness, softness and chemical composition of the biomaterial surface itself.²⁶ We may argue that

the reduced cell adhesion on the films may be due to their lower surface wettability and higher flatness. Some differences were also observed between the films, being f-P(BS80BDG20) surface slightly more hydrophilic than f-PBS. However, no difference in cell growth was observed between a- and r-electrospun mats, suggesting that, for wettable surfaces, viability is not fully related to the material chemical composition.

Cells can attach to surfaces by introducing focal adhesion centres as anchorage. Furthermore, cells preferentially adhered on nanofibers and their orientation was shown to be influenced by fiber alignment.^{27–29} To quantitatively evaluate cell attachment, SAOS-2 cells seeded on the different mats and the control (TCPS) were incubated for 24 h, and the activation of signalling molecules such as FAK and phosphorylated FAK (pY397) was evaluated (Fig. 5B and C). Interestingly, a very faint signal for pFAK was observed on both a- and r-PBS, whereas a-P(BS80BDG20) displayed the highest signal among the studied materials, followed by the control (TCPS) and r-P(BS80BDG20). Our immunoblotting data quantitatively evidenced FAK activity upregulation *via* nanofibrous cultures, in particular for a-P(BS80BDG20) that resulted more suitable for early cell/biomaterial interaction. Indeed, the physico-mechanical processes that regulate early cell–biomaterial interaction are highly important as well as the influence of integrin that mediates cellular adhesion in bone regeneration.³⁰ Previous

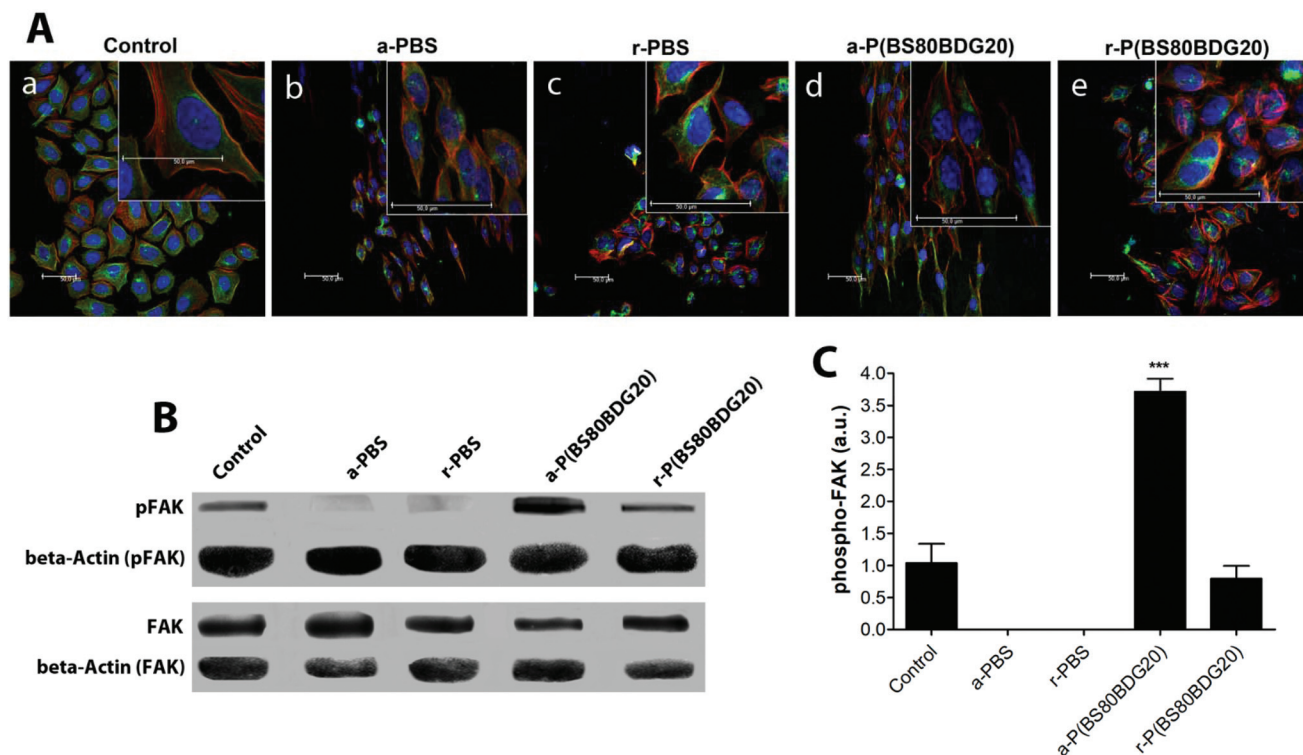


Fig. 5 Cell morphology and quantitative analysis of Focal Adhesion Kinase (FAK) phosphorylation (pFAK) of SAOS-2 on electrospun nanofibers. (A) Representative CLSM images of SAOS-2 cytoskeleton on glass disks (as control) and on electrospun nanofibers of both PBS and P(BS80BDG20) at day 1: adherent cells were fixed, permeabilized and immunostained against F-actin (in red), and beta-tubulin (in green). Nuclei were counterstained with Hoechst 33342 (see details in the Experimental section). Scale bars represent 50 μm . (B) After culturing SAOS-2 for 1 day on control (TCPS) and on electrospun nanofibers of both PBS and P(BS80BDG20), cells were lysated (as described in Experimental section) and their proteins separated by SDS-PAGE. The proteins were transferred to nitrocellulose membranes by Western Blotting (WB) and probed with anti β -actin, anti FAK and anti pFAK (pTyr397 specific) antibodies. Detection was performed with appropriate peroxidase-labelled secondary antibodies in TBS-T buffer and an enhanced chemiluminescence (ECL) kit. (C) Intensity analysis of WB bands was performed with ImageJ software. Results are presented as pFAK/FAK ratio after normalization to beta-actin. Statistical significance values are indicated as *** $p < 0.001$.

studies reported FAK upregulation with nanofibers^{28,31} even if the biomaterial type, nanofiber architecture, diameter, presence of soluble factors and cells were diverse. In our study, contrary to other authors,²⁹ the FAK expression and phosphorylation in SAOS-2 cells cultured on a- and r-nanofibers of similar diameter could not be compared with films with the same surface chemistry since the low level of cell attachment did not allow for protein extraction and immunoblotting experiment. However, it must be underlined that the polymer chemistry of the electrospun scaffolds, combined with the nanofiber orientation, was shown to be biologically quite important. Indeed, aligned electrospun nanofibers of P(BS80BDG20) showed the highest level of FAK expression and phosphorylation in comparison with all nanofibers. The P(BS80BDG20) mat may change the cell microenvironment and ECM, triggering the phosphorylation of focal adhesion kinase (FAK) at Y397, stimulating cell adhesion and proliferation. Under these experimental conditions, the results suggest that focal adhesion signalling may be triggered *via* potential intrinsic effects exerted by the combined action of aligned nanofiber architecture and polymer chemical composition of the P(BS80BDG20) electrospun mat.

The chemical composition of P(BS80BDG20) differs from that of PBS because of the presence of an ether oxygen-atom in its repeating unit. Since ethers have nonbonding electron pairs on their oxygen atoms, they can form hydrogen bonds with other molecules (alcohols, amines, *etc.*) that have O–H or N–H bonds. This property is quite important for cell adhesion. *In vitro*, most mammalian cells are anchorage-dependent and attach firmly to the substrate using specific interactions. The presence of ether-oxygen atoms may confirm the “cell adhesion model”: the more a cell sticks to a substrate, the higher the number of chemical bonds formed.³² Adhesion plays an integral role in cell communication and regulation, and in the development and maintenance of tissues. The affinity of cells to the substrate is a crucial consideration in biomaterial design and development. The process of static *in vitro* cell adhesion is characterized by three stages: attachment of the cell to its substrate (initial stage), cell flattening and spreading, and formation of focal adhesion between the cell and its substrate. It may be possible that the presence of ether-oxygen atoms on the P(BS80BDG20) electrospun mat could allow the formation of a higher number of bonds with the cell membrane components favoring the initial cell attachment. A

recent paper reported how the plasticity of hydrogen bond networks regulates the mechanochemistry of cell adhesion complexes, suggesting that nature uses a ductile network of hydrogen bonds to engineer function over a broad range of forces.³³

On the other hand, since it is known that cells cultured on an aligned electrospun fibrous substrate exhibit contact guidance, we cannot ignore that the presence of ethers along the P(BS80BDG20) backbone may allow a better nanofiber alignment in comparison with PBS (0.66 vs. 0.77), thanks to the formation of more interchain bonds. Both factors may therefore contribute to improving the cell attachment on P(BS80BDG20) electrospun mats.

2.4. Osteoblasts differentiation

Cell viability during the culture period was determined through an MTT test performed on days 7 and 14 and at the end of the culture period (21 days). The average cell viability of all samples was in the 80%–98% range without statistically significant differences ($p > 0.05$) in comparison with the control (TCPS) (data not shown). A slight increment in cell viability

was observed on a-P(BS80BDG20) with respect to the other scaffolds. At day 21, all samples were analysed for bone gene expression and calcified extracellular matrix deposition.

2.4.1. Characterization of bone gene expression. A qRT-PCR analysis for the gene expression profile of bone-specific proteins was carried out at 21 days using the $\Delta\Delta Ct$ method. The results showed some specific differences in alkaline phosphatase (ALP), osteocalcin (OSC) and bone sialoprotein (BOSP) ($p < 0.05$) gene expressions in comparison with the control (TCPS) that was set equal to 1 (data not shown) (Fig. 6). In general, the increase in gene expression was more marked for cells cultivated on either a- and r-P(BS80BDG20) than on both PBS nanofibers. ALP gene expression showed almost 4- and 2-fold induction increment on both a- and r-P(BS80BDG20), respectively (a- vs. r-P(BS80BDG20), $p < 0.05$). On the other hand, on PBS nanofibers the results were quite different. ALP on a-PBS was significantly reduced in comparison with r-PBS (a- vs. r-PBS, $p < 0.05$). For OSC the trend was quite similar to ALP even if the fold increase was lower (a- vs. r-P(BS80BDG20), $p < 0.05$). Also, for BOSP the induction was almost 6- and more than 3-times higher on a- and r-P(BS80BDG20), respectively (a- vs. r-P(BS80BDG20), $p < 0.05$). On a-PBS, the increment was almost 3-fold with respect to r-PBS (a- vs. r-PBS, $p < 0.05$). Lastly, no evident differences were detected for the expression of the other bone proteins ($p > 0.05$) (data not shown).

In conclusion, the qRT-PCR analysis showed an increase in ALP, OSC and BOSP expression levels on both a- and r-P(BS80BDG20) in comparison with a- and r-PBS. The increase in the transcript levels of ALP, OSC and BOSP genes was supported by protein deposition (Table 2) and mineralization data (Fig. 8).

2.4.2. Characterization of the calcified extracellular matrix deposition. In order to evaluate the amount of extracellular matrix constituents produced throughout all nanofibrous mats, an ELISA assay of the extracted extracellular matrix was performed (Table 2). At day 21, the deposition of most part of the evaluated bone proteins throughout the electrospun nano-

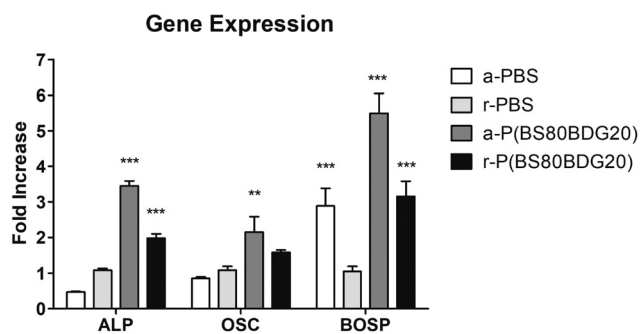


Fig. 6 Gene expression of the indicated bone-specific markers as determined by qRT-PCR on electrospun nanofibers. SAOS-2 were seeded and cultured in osteogenic medium on electrospun nanofibers of both PBS and P(BS80BDG20) for 21 days. The graph shows the fold increase of gene expression related to cells grown onto control (TCPS). Statistical significance values are indicated as $**p < 0.01$; $***p < 0.001$.

Table 2 Protein titration of bone ECM produced by SAOS-2 cultured for 21 days in osteogenic medium on electrospun nanofibers of both PBS and P(BS80BDG20). Results are expressed as protein (pg) per cell \times disk and presented as the average \pm standard deviation for three measurements in two separate experiments. In the table the internal ratio (fourth column) of both a-PBS vs. r-PBS and a-P(BS80BDG20) vs. r-P(BS80BDG20) electrospun nanofibers is indicated. In the fifth column, the ratio of a-P(BS80BDG20) vs. a-PBS and of r-P(BS80BDG20) vs. r-PBS is also reported. Statistical significance values are indicated as: $*p < 0.05$; $**p < 0.01$; $***p < 0.001$

Proteins	Control (TCPS)	PBS		P(BS80BDG20)		Ratio aligned/random (a/r)		Ratio P(BS80BDG20)/PBS	
		Aligned	Random	Aligned	Random	PBS	P(BS80BDG20)	Aligned	Random
ALP	40.32 \pm 2.32	26.09 \pm 5.32	39.47 \pm 1.57	86.42 \pm 3.20	36.58 \pm 6.15	0.66	2.36***	3.31***	0.93
hFn	40.25 \pm 3.21	30.07 \pm 1.13	39.00 \pm 1.03	84.94 \pm 10.53	46.40 \pm 1.82	0.77	1.83***	2.82***	1.19
OSC	305.62 \pm 5.23	324.15 \pm 0.22	364.55 \pm 0.01	463.42 \pm 0.01	232.42 \pm 0.011	0.89	1.99***	1.43*	0.64
ONT	7.36 \pm 0.89	7.18 \pm 1.03	9.05 \pm 1.23	9.76 \pm 0.96	8.30 \pm 1.11	0.79	1.18*	1.36**	0.92
OPN	356.23 \pm 5.23	411.2 \pm 26.04	314.3 \pm 47.87	535.60 \pm 72.37	341.15 \pm 60.25	1.31**	1.57***	1.30**	1.09
DCN	752.35 \pm 21.37	893.8 \pm 25.03	534.84 \pm 26.30	1812.8 \pm 5.41	413.87 \pm 12.86	1.67***	4.38***	2.03***	0.77
Type-I Coll	1005.62 \pm 29.48	1195.5 \pm 12.91	938.3 \pm 152.7	1450.5 \pm 11.93	932.8 \pm 206.89	1.27	1.55***	1.21**	0.99
Type-III Coll	1058.24 \pm 19.63	1989.4 \pm 22.3	1970.4 \pm 136.3	2048.28 \pm 43.7	1860.9 \pm 50.07	1.01	1.10*	1.03	0.94

fibrous samples was considerably enhanced ($p < 0.05$) in comparison with the control (Table 2). The bone proteins deposited on a-PBS showed a significant increment only for osteopontin (OPN) and decorin (DCN) in comparison with r-PBS ($p < 0.05$). Interestingly, the enhancement was significantly evident for all proteins (hFn, ALP, OSC, ONT, OPN, DCN, Type-I Coll and Type-III Coll) on a-P(BS80BDG20) in comparison with r-P(BS80BDG20) ($p < 0.05$). Furthermore, the extracellular matrix deposited on a-P(BS80BDG20) was significantly higher with respect to a-PBS ($p < 0.05$) (Table 2). All these proteins produced by cells as organic components of ECM represent important markers of bone formation and remodelling. Type-I collagen synthesis is upregulated at the proliferation stage and downregulated during the subsequent stages, type-III collagen, a fibrous scleroprotein in bone, is frequently observed in association with type-I collagen, and decorin, a member of a small leucine rich repeat family of proteoglycans, colocalizes with collagen, aids the assembly of collagen fibers and regulates HA crystal growth.³⁴ FN is an adhesive glycoprotein and it is known to be involved in the early stages of osteogenesis.³⁵ The higher value of deposited Fn on a-P(BS80BDG20) in comparison with the other mats may facilitate both adhesion and differentiation of osteoblasts. Osteonectin (ONT) is a calcium and collagen binding ECM glycoprotein and modulates cell–matrix interactions,³⁶ whereas osteopontin (OPN), an extracellular protein showing a cell-adhesion sequence (RGD) that mediates its interaction with integrin and extracellular matrix components is involved in bio-mineralization and remodelling of bone, chemotaxis, apoptosis and cell activation in immunity.³⁷ Decorin (DCN) represents an osteoblasts terminal differentiation marker,³⁸ while osteocalcin (OSC), the most abundant noncollagenous protein of the bone matrix, is released by differentiated osteoblasts during bone formation and binds with the mineralized bone matrix.³⁹ Furthermore, OSC is a late marker of osteoblastic differentiation that is closely related to osteoblastic maturation and matrix mineralization.

It is worth highlighting that the difference in protein expression for both r-PBS and r-P(BS80BDG20) is not significant, indicating a lower effect of material chemical composition of r-ES on SAOS-2 cell differentiation ($p > 0.05$) (Table 2). The ability to form an extracellular matrix that can undergo regulated mineralization is the ultimate phenotypic expression of an osteogenic tissue: a-P(BS80BDG20) seems to respond quite well to this request.

Fig. 7 shows ALP activity determined on nanofibrous mats at the end of the culture period expressed as percentage related to the control (TCPS). The level of ALP activity was consistently higher on a- than on r-P(BS80BDG20) ($p < 0.05$). ALP activity was also statistically different between a- and r-PBS ($p < 0.05$), although the trend is the opposite with respect to P(BS80BDG20). Indeed, the ALP activity was lower for a-PBS in comparison to r-PBS (Fig. 7). In summary, the ALP value was quite similar for both r-PBS and r-P(BS80BDG20), whereas a lower value was observed for a-PBS. These results seem to indicate that ALP activity is not affected by the different chemistry

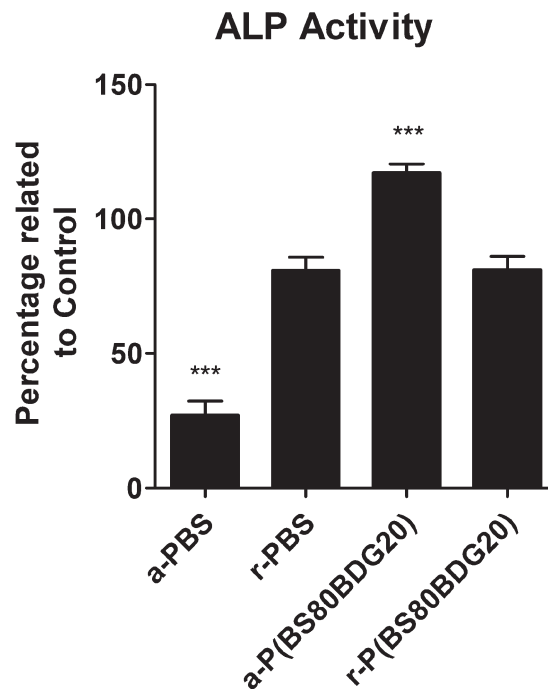


Fig. 7 Alkaline phosphatase (ALP) specific activity of SAOS-2 on electrospun nanofibers. At day 21, ALP activity was determined calorimetrically, corrected for the protein content measured with the BCA Protein Assay Kit and expressed as percentage related to TCPS (control) for both a- and r-nanofibers of either PBS and P(BS80BDG20). Bars express the mean values \pm SEM of results from three experiments in two separated experiments. Statistical significance values are indicated as *** $p < 0.001$.

of the mats if the nanofibers are randomly distributed; a great difference in ALP activity is manifest when the chemistry of the mats is associated with the nanofiber alignment, being more favourable for P(BS80BDG20) mats. In conclusion, if the cell viability resulted almost similar on both types of mats, the activity of ALP, the marker of osteoblast differentiation, was more affected by the chemistry of the mat associated with the nanofiber orientation. This suggests that when both factors act in a synergistic mode, they may promote osteoblast differentiation. From an applicative point of view, this result becomes very important.

The relative amount of matrix calcification on both PBS and P(BS80BDG20) mats was evaluated by CLSM observation (Fig. 8A) and the calcium–cresolphthalein complexone method (Fig. 8B). Fig. 8A is a representative CLSM image of day 21 of cell culture on both PBS and P(BS80BDG20) mats analyzed for calcium deposition (green fluorescent dots). The presence of a higher amount of calcium deposition on either a- and r-P(BS80BDG20) in comparison with both PBS mats can be observed. Fig. 8B shows that the mineralization of the extracellular matrix produced by SAOS-2 cells was considerably greater on a- than on r-P(BS80BDG20) ($p < 0.05$). Again, as for ALP protein level and enzymatic activity, calcium matrix deposition was statistically reduced on a-PBS in comparison with r-PBS ($p < 0.05$) (Fig. 8B). Interestingly, the increase in calcium deposition was consistent with the higher ALP expression

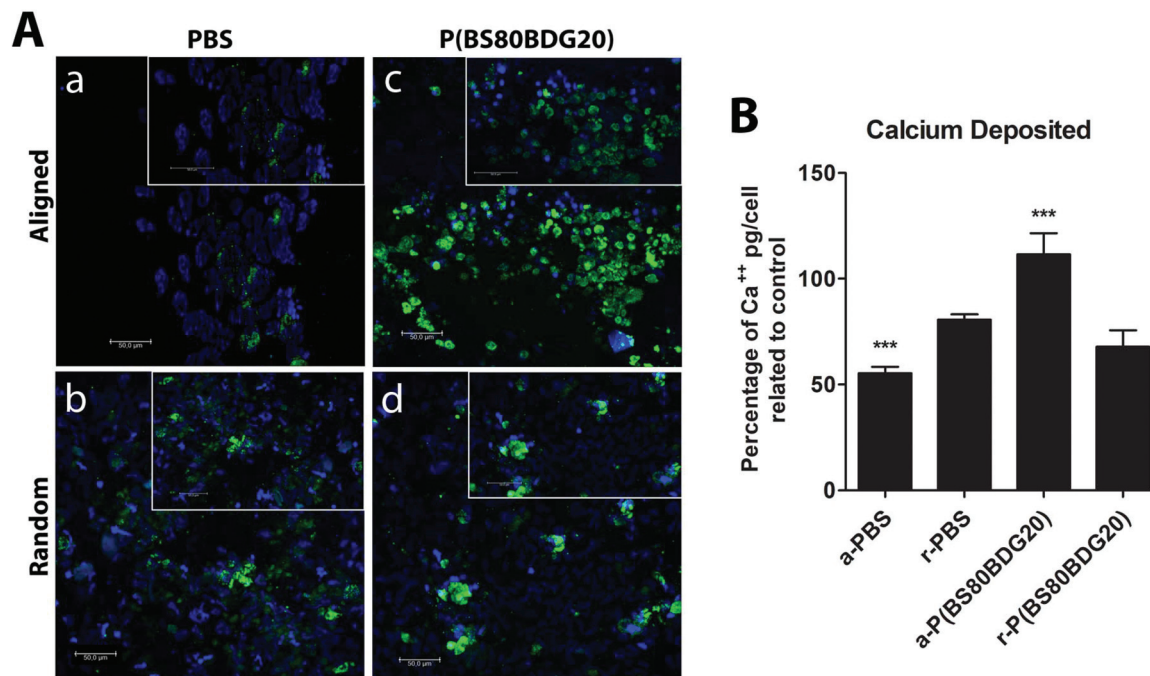


Fig. 8 Calcium deposition of SAOS-2 on electrospun nanofibers. (A) Representative CLSM images at 20 \times of calcium deposited by SAOS-2 cells cultured for 21 days on a- and r-electrospun nanofibers of both mats. Scale bars represent 50 μm . (B) Mineralization of extracellular matrix produced by SAOS-2 cells seeded on TCPS (control) and on electrospun nanofibers of both PBS and P(BS80BDG20) as determined by quantification of calcium content. Results are expressed as percentage of pg Ca^{2+} per cell related to TCPS (control). The data are presented as the average \pm standard deviation for three measurements in two separate experiments. Statistical significance values are indicated as *** $p < 0.001$.

solely on a-P(BS80BDG20): in fact, the protein content was two-fold greater than that on the control (Table 2). As previously indicated (Fig. 7), an increase in the ALP activity was detected on a-P(BS80BDG20) scaffolds. Since the mineralization of the matrix is initiated by the expression of the membrane-bound glycoprotein ALP on the osteoblasts, both the elevated gene and protein expressions of ALP may suggest that the osteoblasts on a-P(BS80BDG20) are more differentiated than those on the other mats, and have already started to promote bone ECM deposition. Again, we may argue that for osteoblast differentiation both the chemistry of the mats and the nanofiber alignment played a crucial role, being more favourable for a-P(BS80BDG20).

3. Conclusions

PBS and P(BS80BDG20) based nanofibrous scaffolds of similar and uniform size were successfully prepared by electrospinning. The presence of BDG co-units along the PBS backbone caused a significant decrement of the overall degree of crystallinity that resulted in a significant enhancement of the hydrolysis rate, when incubated in phosphate buffer at 37 $^{\circ}\text{C}$ for about 7 months.

In vitro biological assays were performed with human SAOS-2 cells, a widely used and well-accepted model for osteoblast study. In comparison with both f-PBS and f-P

(BS80BDG20), SAOS-2 cell viability was greater on all ES scaffolds. SEM observations confirmed cell adhesion on either a- or r-nanofibers of both PBS and P(BS80BDG20) scaffolds. The quantification of phosphorylated FAK expression delineated a-P(BS80BDG20) electrospun scaffolds as the most suitable for early cell–biomaterial interaction in comparison with random mats. Cell osteogenic differentiation was also higher on a-P(BS80BDG20) scaffolds with respect to the other tested materials. The presence of ether-oxygen atoms along P(BS80BDG20) electrospun nanofibers may allow a greater cell adhesion in comparison with PBS. From a chemical point of view, the structure of PBS and P(BS80BDG20) presents some crucial differences (Fig. 1). Indeed, the P(BS80BDG20) repeating unit is characterized by the presence of one ether bond, absent in PBS. This leads to an increased density of hydrogen bond acceptors along the P(BS80BDG20) backbone with respect to PBS, which in turn can interact with cell membrane components, causing a better cell attachment on the copolymer mats. For the same reason, *i.e.* the presence of ether linkages along the copolymer macromolecular chain, P(BS80BDG20) is capable of stronger interchain interactions with respect to the PBS homopolymer. This is confirmed by the increase of the glass transition temperature of the first as compared to the latter. The finding has already been described in the literature for this and other similar copolymeric systems.^{18,40,41} From a biochemical point of view, we may argue that since P(BS80BDG20) contains ether linkages, on the

one hand the formation of hydrogen bonds with cell membrane components (receptor, integrins and focal adhesion molecules) involved in the initial cell attachment is highly probable. On the other hand, the higher number of interchain bonds between the electrospun nanofibers should allow for a better alignment useful for cell contact guidance, adhesion and proliferation. Both the previous indicated interactions could equally contribute to improving cell adhesion on a-P (BS80BDG20). The novel aligned nanoelectrospun mats based on the P(BS80BDG20) copolymer seem indeed to provide a favorable environment for osteoblast proliferation and function by supporting enhanced ECM deposition and mineralization.

In conclusion, all the findings demonstrated how the addition of ether-oxygen atoms along the PBS backbone is a simple, yet winning strategy to significantly promote the biological interaction, without the need for any further material manipulation (*e.g.* surface functionalization and/or addition of fillers for composite fabrication). Thus, these outcomes may open up new scenarios for the preparation of materials specifically tailored for (bone) tissue regeneration.

4. Experimental

4.1. Polymer synthesis

Dimethylsuccinate (DMS), 1,4-butanediol (BD), diglycolic acid (DGA), and titanium tetrabutoxide (TBT) (Sigma-Aldrich) were reagent grade products. All the reagents were used as supplied with the exception of TBT, which was distilled before use.

Poly(butylene succinate) (PBS) and poly(butylene succinate/diglycolate) (P(BS80BDG20)) were respectively synthesized by two-step melt polycondensation from BD and DMS and from BS, DMS (80%) and DGA (20%), as previously reported.¹⁸ Ti(OBu)₄ was employed as a catalyst (about 150 ppm of Ti per g of polymer) and 20 mol% excess of BD with respect to DMS (or DMS and DGA) was used. The first stage, under nitrogen flow, was run at 180 °C until the theoretical amount of methanol was distilled off. In the second stage, the pressure was reduced to about 0.1 mbar and the temperature was increased to 200 °C. The polymerizations were carried out until a constant torque value was measured.

4.2. Production and characterization of films and electrospun scaffolds (ES)

4.2.1. Fabrication. Thin films of about 200 μm thickness were obtained by compression molding of PBS and P(BS80BDG20) (hereinafter called f-PBS and f-P(BS80BDG20), respectively). Polymer powders were placed in press (Carver C12, laboratory press) in between two Teflon plates and heated to 140 °C. After melting, a constant pressure of 2 ton per m² was applied for 2 min. Films were cooled to room temperature in press using tap water.

For scaffold fabrication, polymer powder was dissolved in 1,1,1,3,3,3-hexafluoro-2-propanol with a final concentration of 15% (w/v) and stirred overnight at room temperature to obtain

a homogeneous solution before electrospinning. Electrospinning was carried out at room temperature and a relative humidity level of 30%. Polymer solutions were loaded into a syringe and controlled using a pump at a feeding rate of 0.3 ml h⁻¹ and 2 ml h⁻¹ for PBS and P(BS80BDG20), respectively. The distance between the needle tip and the collector was set at a constant value of 15 cm and the applied voltage was 18 kV. To produce random fibers of both PBS and P(BS80BDG20) (hereinafter called r-PBS and r-P(BS80BDG20), respectively), a flat metal plate was used to collect fibers. For aligned fibers of both PBS and P(BS80BDG20) (hereinafter called a-PBS and a-P(BS80BDG20), respectively) a mandrel with a rotation speed of 6000 rpm min⁻¹ was employed.

4.2.2. Molecular, thermal and structural characterization.

Molecular weights were evaluated by gel-permeation chromatography (GPC) at 30 °C using a 1100 HPLC system (Agilent Technologies, USA) equipped with a PLgel 5 mm MiniMIX-C column (Agilent Technologies, USA). A refractive index was employed as a detector. Chloroform was used as an eluent with a 0.3 mL min⁻¹ flow and a sample concentration of about 5 mg mL⁻¹.

Thermogravimetric analysis (TGA) was performed under a nitrogen atmosphere using a PerkinElmer TGA7 apparatus (gas flow: 30 mL min⁻¹) at 10 °C min⁻¹ heating rate up to 800 °C.

Calorimetric measurements were carried out by means of a PerkinElmer DSC7 instrument. The external block temperature control was set at -80 °C and weighed samples of about 10 mg encapsulated in aluminium pans were heated up to 40 °C above the fusion temperature at a rate of 20 °C min⁻¹. The degree of crystallinity (X_c) was calculated using the following equation:

$$X_c = \frac{\Delta H_m}{\Delta H_m^0} \times 100 \quad (1)$$

where ΔH_m is the melting enthalpy associated with the first heating scan and ΔH_m^0 is the theoretical melting enthalpy of the 100% crystalline PBS homopolymer, equal to 200 J g⁻¹.⁴²

Static contact angle measurements were performed on polymer films using a KSV CAM101 (KSV, Espoo, Finland) instrument at room temperature by recording the side profiles of deionized water drops for image analysis. Five drops were observed on different areas for each film, and contact angles were reported as the average value ± standard deviation.

Fiber morphology was investigated by using an XL 30 ESEM-FEG (Philips, The Netherlands) scanning electron microscope (SEM). The samples were sputter coated with gold before imaging. The imaging was performed at an accelerating voltage of 10 kV. Fiber diameter was analyzed using Photoshop CS4 by measuring at least 100 fibers, taken from a minimum of 4 SEM images at random locations. The fiber orientation was evaluated by using the Orientation J plugin, providing a coherence value from 0 (completely random) to 1 (perfectly aligned)⁴³ and by creating a FFT image of the SEM micrograph.⁴⁴

4.2.3. Hydrolytic degradation. Hydrolysis studies were carried out on ES mats (10 × 35 mm, 200 μm thick) individually immersed in phosphate buffered solution (0.1 M, pH 7.4) and incubated in an SW22 Julabo shaking water bath at 37 °C and 50 rpm. Buffer solution was periodically changed to keep the pH constant during the entire time scale. Prior to experiments, each specimen was dried over P₂O₅ under vacuum at room temperature to constant weight and then weighed to obtain the sample initial mass. At different time intervals, duplicate sacrificial specimens of each sample were repeatedly washed with deionized water and dried over P₂O₅ under vacuum for 2 days to constant weight. The mass loss was determined gravimetrically.

4.3. Biological experiments

4.3.1. Cell seeding and culture conditions. The human osteoblast cell line SAOS-2 was obtained from the American Type Culture Collection (HTB85, ATCC, Manassas, VA, USA). The cells were routinely cultured in flasks with McCoy's 5 A modified medium containing L-glutamine and HEPES (Cambrex Bio Science, Baltimore, MD, USA), supplemented with 15% foetal bovine serum, 2% sodium pyruvate, and 1% antibiotics (proliferative medium, PM). For the experiments, cells were detached by treatment with trypsin-EDTA (Cambrex Bio Science, Baltimore, MD, USA) and counted.

Flat films and electrospun nanofibers were sterilized by ethylene oxide at 38 °C for 8 h at 65% relative humidity. After 24 h aeration in order to remove the residual ethylene oxide, specimens were placed inside a standard 24-well-plate and were washed with sterile distilled water followed by 0.9% NaCl sterile solution and finally cell culture medium. A cell suspension of 2 × 10⁵ cells was placed on top of each scaffold. After 0.5 h of incubation, 1 mL of culture medium was added. Two different studies were performed as indicated.

Biocompatibility studies: cells seeded on films and electrospun nanofibers were cultured in PM for 1, 3 and 7 days, respectively. Cell viability, Annexin V staining, adhesion and morphology were evaluated.

Differentiation studies: cells seeded on aligned and random electrospun mats were cultured in osteogenic medium (OM) for 3, 7 and 21 days, respectively. In detail, OM was composed of PM with the addition of 10⁻⁸ M dexamethasone and 10 mM β-glycerophosphate (Sigma-Aldrich, St Louis, MO, USA).⁴⁵ Ascorbic acid, another osteogenic supplement, is already a component of McCoy's 5A modified medium. Cell viability, gene expression analysis, quantification of the bone calcified extracellular matrix and evaluation of ALP activity were determined.

For both studies, SAOS-2 were seeded on tissue culture plate (TCPS) wells, cultured under PM or OM conditions for the above indicated time intervals and used as the control.

4.3.2. Cell viability. A resazurin-based assay was used to estimate the number of viable cells by measuring the reduction of resazurin into resorufin. A resazurin solution (Sigma-Aldrich) was added in a 1 : 10 ratio with respect to the culture volume to each well of the plate, and incubated for 3 h at 37 °C with 5% CO₂. At the end of the incubation time, the

absorbance was measured at 595 and 695 nm wavelengths using a microplate reader (Bio-Rad Laboratories, Hercules, CA).

Biocompatibility studies: cell viability was evaluated on cells seeded on films and electrospun scaffolds for the above indicated times.

Differentiation studies: cell viability was determined on electrospun nanofibers cultured under OM conditions for 3, 7 and 21 days, respectively. In this case, films were not used, as they did not show good biocompatibility performances. A standard cell viability curve was used and the results were expressed as percentage of the control (TCPS), set as 100%.

4.3.3. Annexin V staining. The annexin V technique detects apoptosis by targeting the loss of phospholipid asymmetry in the plasma membrane. The loss of plasma membrane asymmetry is an early event in apoptosis, independent of cell type, resulting in the exposure of phosphatidylserine (PS) residues at the outer plasma membrane leaflet.⁴⁶ To determine apoptosis, SAOS-2 cells were seeded and incubated for 24 h on films and electrospun scaffolds at 37 °C. After incubation, the adherent SAOS-2 were labelled using the PSVue480™ cell stain according to the manufacturer's instructions (Molecular Targeting Technologies, Inc., PA, USA). The experiment was performed as previously described.⁴⁷

4.4. Morphological analysis and cell adhesion

4.4.1. Scanning electron microscopy (SEM) observation. SAOS-2 morphological observations were performed after 1 and 7 days of culture in PM. Cells (1 × 10⁵) cultivated on films, electrospun scaffolds and on thermanox disks (as a control) were fixed with a 2.5% (v/v) glutaraldehyde solution in 0.1 M Na-cacodylate buffer (pH 7.2) for 1 h at 4 °C and washed with Na-cacodylate buffer. Afterwards, samples were dehydrated at room temperature in an EtOH gradient for 15 min and then critical point-dried with CO₂. A Zeiss EVO MA10 (Carl Zeiss, Oberkochen, Germany) was used. The samples were gold-sputter coated under nitrogen to render them electrically conductive prior to microscopy. Magnification was at 3000× and 5000× for each sample.

4.4.2. Confocal laser scanning microscopy (CLSM) analysis. For cell morphological analyses and focal adhesion quantification, SAOS-2 cells (1 × 10⁵) were cultivated in PM on glass disks (control) and electrospun nanofibers for 24 h.

Morphological studies. Cells were extensively washed with saline solution (0.9%), fixed with paraformaldehyde (0.4% in PBS) for 30 min and then permeabilized with 0.1% Triton X-100 for 10 min at room temperature (RT). At the end of this treatment, the cells were incubated with phalloidin (Alexa-Fluor-488 phalloidin, Invitrogen) for 20 min and then with anti-tubulin (Alexa-Fluor 633, Invitrogen) for 1 h at RT. All samples were mounted and nuclei were counterstained with Hoechst (Sigma Aldrich). The images were taken using a TCS SPII confocal microscope (Leica Microsystems, Bensheim, Germany) equipped with a digital image capture system at 20× and 40× magnification.

Focal adhesion quantification. Cells were scraped from the samples and lysed with ice-cold lysis buffer (50 mM Tris pH

7.5, 50 mM NaCl, 5 mM ethylenediaminetetraacetic acid, 0.1% Triton, and 1 mM sodium orthovanadate) for 30 min on ice. The lysates were centrifuged at 12 000 rpm for 5 min at 4 °C, and supernatant protein concentrations were determined by a bicinchoninic acid assay (BCA, a Thermo Scientific Pierce BCA Protein Assay Kit). Equivalent samples were subjected to SDS-PAGE on 8% gel. Proteins were then transferred onto nitrocellulose membranes, blocked with 2% BSA in phosphate buffer for 1 h at RT and probed with the primary antibodies FAK (diluted 1 : 500) and anti-phosphorylated FAK (pY397) (diluted 1 : 500) or anti-beta-actin (diluted 1 : 500) from Santa Cruz Biotechnologies (Santa Cruz, CA, USA), overnight at 4 °C. Samples were then incubated with secondary antibodies conjugated to HRP (1 : 1000) for 1 h at RT. Detection was performed with an ECL solution and revealed by autoradiography using an ImageQuant LAS4000 Imaging System (GE Healthcare). Densitometry analysis of the band was carried out using Image™ software. The bands were then quantified by densitometric analysis.

4.5. Differentiation studies

4.5.1. Gene expression analyses. Total RNA from SAOS-2 cells cultured on electrospun nanofibers and the control (TCPS) in osteogenic medium for 21 days was extracted with Trizol reagent (Invitrogen) and retrotranscribed into cDNA with an iScript cDNA Synthesis Kit (Bio-Rad Laboratories) as previously reported.⁴⁸ Total RNA was extracted from cells cultured under OM conditions. A quantitative reverse-transcription polymerase chain reaction (qRT-PCR) analysis was performed in a 48-well optical reaction plate using a MiniOpticon Real-Time PCR System (Bio-Rad Laboratories). Oligonucleotide primers were designed with gene sequences published in GenBank and are indicated in Table S1.† Reactions were performed in 20 µL with 2 µL of cDNA, 10 µL Brilliant SYBER Green qPCR Master Mix (Bio-Rad Laboratories), 0.4 µL of each primer, and 7.2 µL H₂O. The PCR conditions were as follows: 3 min at 95 °C, 30 cycles of 5 s at 95 °C, and 23 s at 60 °C. Gene expression was normalized to the GAPDH housekeeping gene expression. Each sample was analysed in triplicate and correlated against a standard curve. The reaction mixture without cDNA was used as a negative control in each run.

4.5.2. Purified proteins and polyclonal antisera. Decorin, type-I collagen, and fibronectin were purified as previously described.⁴⁸ Osteocalcin was acquired from Biomedical Technologies, Inc. (Stoughton, MA), osteopontin and osteonectin were obtained from Assay Designs, Inc. (Ann Arbor, MI), and type-III collagen and ALP were purchased from Sigma-Aldrich, Inc.

Dr Larry W. Fisher (<http://csdb.nidcr.nih.gov/csdb/antisera.html>, National Institutes of Health, Bethesda, MD) provided us with the rabbit polyclonal anti-type-I and -III collagen, anti-decorin, anti-osteopontin, anti-osteocalcin, anti-osteonectin, and anti-ALP. A polyclonal antibody against human fibronectin was produced as previously described.⁴⁹

4.5.3. Bone protein extraction and ELISA assays. To evaluate the amount of ECM produced by SAOS-2 on electrospun nanofibers and the control (TCPS), the samples were washed extensively with sterile phosphate buffer and then incubated

for 24 h at 37 °C with 1 mL of sterile sample buffer (20 mM Tris-HCl, 4 M GuHCl, 10 mM EDTA, 0.066% [w/v] sodium dodecyl sulfate [SDS], pH 8.0). At the end of the incubation period (21 days), the total protein concentration was determined with a BCA Protein Assay Kit (Pierce Biotechnology, Inc., Rockford, IL). In detail, the protein concentration for cells cultivated under OM conditions was 264.32 ± 5.24 µg for cells on TCPS wells, 315.69 ± 7.56 µg on r-PBS and 326.54 ± 8.52 µg on a-PBS, whereas it was 295.45 ± 5.38 µg on r-P (BS80BDG20) and 321.56 ± 6.34 µg on a-P(BS80BDG20), respectively. The protein amount obtained from cells cultivated under PM conditions was quite similar, but the specific bone protein was undetectable by the ELISA assay. Calibration curves to measure type-I and -III collagens, decorin, osteopontin, osteocalcin, osteonectin, fibronectin and ALP were prepared as previously described.⁵⁰ To measure the ECM amount of each protein, an enzyme-linked immunosorbent assay (ELISA) was performed as reported in the literature.⁵⁰ The amount of ECM constituents from both samples was expressed as pg per (cell × disk).

4.5.4. ALP activity. ALP activity was determined using a colorimetric endpoint assay at day 21. The assay measures the conversion of the colourless substrate *p*-nitrophenol phosphate (PNPP) by the enzyme ALP into the yellow product *p*-nitrophenol; the rate of colour change corresponds to the amount of enzyme present in the solution. The test was performed as previously described on cells cultured on electrospun scaffolds and the control at day 21.⁵⁰ Samples were analyzed in triplicate and compared with the calibration curve of *p*-nitrophenol standards. Enzyme activity was determined as micromoles of *p*-nitrophenol produced per minute per milligram of enzyme. Finally, the data were expressed as percentage of enzyme activity as compared to TCPS (control).

4.5.5. Quantification of calcium deposits. To evaluate the calcium deposition, fluorescent calcein detection and calcium-cresolphthalein complexone method were performed on SAOS-2 seeded on electrospun scaffolds and TCPS wells as described in the literature.⁵¹

Fluorescent calcein detection. At the end of cell incubation (21 days), specimens were rinsed with sterile phosphate buffer and stained with a calcein solution (5 mM in phosphate buffer; Invitrogen, Carlsbad, CA) for 30 min at 22 °C. The samples were counterstained with a Hoechst 33342 (Sigma) solution ($2 \mu\text{g mL}^{-1}$) to target the cellular nuclei, and then washed with phosphate buffer. Images were taken using a TCS SPII confocal microscope (Leica Microsystems) equipped with a digital image capture system at 20× magnification.

Calcium-cresolphthalein complexone method. To evaluate calcium deposition, the calcium-cresolphthalein complexone method was performed on SAOS-2 seeded on different samples at 21 days of culture. Briefly, the calcium content of each sample was assayed to quantify the amount of mineralized matrix, using a Calcium Fast kit (Mercury SPA, Naples, Italy) according to the manufacturer's instructions as previously reported.⁵¹ Tests were performed in triplicate and compared with the calibration curve of standards. Firstly, the data were

determined in pg Ca²⁺ per cell and finally expressed as percentage related to the control (TCPS).

No images or calcium quantifications were recorded for cells cultivated under PM conditions since no calcium deposits were observed and detected.

4.6. Statistics

Each experiment was performed in triplicate and in at least two separate experiments. The results are expressed as the mean ± standard deviation. In order to compare the results among all scaffolds, one-way analysis of variance (ANOVA) with a *post hoc* Bonferroni's test was applied, with a significance level of 0.05.

Conflicts of interest

There are no conflicts of interest to declare.

Acknowledgements

LV would like to thank COST Action MP1206 "Electrospun nanofibers for bio inspired composite materials and innovative industrial applications" (2012–2017) (http://www.cost.eu/COST_Actions/mpns/MP1206). We are grateful to P. Vaghi (Centro Grandi Strumenti di Pavia, University of Pavia, Pavia, Italy, <http://cgs.unipv.it/>) for technical assistance in the confocal laser scanning microscopic studies. We also thank Gunel Mustafazade (Azerbaijan), who participated in this study as an Erasmus Mundus student. This project/research has been made possible with the support of the Dutch Province of Limburg (HC and LM).

References

- 1 R. Florencio-Silva, G. Rodrigues da Silva Sasso, E. Sasso-Cerri, M. J. Simões and P. S. Cerri, *BioMed Res. Int.*, 2015, **2015**, 1–17.
- 2 A. R. Amini, C. T. Laurencin and S. P. Nukavarapu, *Crit. Rev. Biomed. Eng.*, 2012, **40**, 363–408.
- 3 K. Chaudhury, V. Kumar, J. Kandasamy and S. RoyChoudhury, *Int. J. Nanomed.*, 2014, **9**, 4153–4167.
- 4 G. G. Walmsley, A. McArdle, R. Tevlin, A. Momeni, D. Atashroo, M. S. Hu, A. H. Feroze, V. W. Wong, P. H. Lorenz, M. T. Longaker and D. C. Wan, *Nanomedicine*, 2015, **11**, 1253–1263.
- 5 M. F. Griffin, D. M. Kalaskar, A. Seifalian and P. E. Butler, *Open Orthop. J.*, 2016, **10**, 836–848.
- 6 Z. Rezvani, J. R. Venugopal, A. M. Urbanska, D. K. Mills, S. Ramakrishna and M. Mozafari, *Nanomedicine*, 2016, **12**, 2181–2200.
- 7 M. Mohammadi, S. A. M. Shaegh, M. Aliboland, M. H. Ebrahimzadeh, A. Tamayol, M. R. Jaafari and M. Ramezani, *J. Controlled Release*, 2018, **274**, 35–55.
- 8 J. Xue, J. Xie, W. Liu and Y. Xia, *Acc. Chem. Res.*, 2017, **50**, 1976–1987.
- 9 B. Sun, Y. Z. Long, H. D. Zhang, M. M. Li, J. L. Duvail, X. Y. Jiang and H. L. Yin, *Prog. Polym. Sci.*, 2014, **39**, 862–890.
- 10 M. Gigli, M. Fabbri, N. Lotti, R. Gamberini, B. Rimini and A. Munari, *Eur. Polym. J.*, 2016, **75**, 431–460.
- 11 C. Gualandi, M. Soccio, M. Govoni, S. Valente, N. Lotti, A. Munari, E. Giordano, G. Pasquinelli and M. L. Focarete, *J. Bioact. Compat. Polym.*, 2012, **27**, 244–264.
- 12 M. Tallawi, R. Rai, M. R. Gleixner, O. Roerick, M. Weyand, J. A. Roether, D. W. Schubert, A. Kozłowska, M. El Fray, B. Merle, M. Goken, K. Aifantis and A. R. Boccacini, *Macromol. Symp.*, 2013, **334**, 57–67.
- 13 M. L. Alves de Silva, A. Crawford, J. M. Mundy, V. M. Correlo, P. Sol, M. Bhattacharya, P. V. Hatton, R. L. Reis and N. M. Neves, *Acta Biomater.*, 2010, **6**, 1149–1157.
- 14 H. Li, J. Chang, A. Cao and J. Wang, *Macromol. Biosci.*, 2005, **5**, 433–440.
- 15 H. Wang, J. Ji, W. Zhang, W. Wang, Y. Zhang, Z. Wu, Y. Zhang and P. K. Chu, *Acta Biomater.*, 2010, **6**, 154–159.
- 16 A. R. Costa-Pinto, I. Vargel, V. M. Correlo, P. C. Sol, S. Faria, E. Piskin, R. L. Reis and N. M. Neves, *J. Biomater. Appl.*, 2014, **28**, 1430–1442.
- 17 H. Chen, M. Gigli, C. Gualandi, R. Truckenmüller, C. van Blitterswijk, N. Lotti, A. Munari, M. L. Focarete and L. Moroni, *Biomaterials*, 2016, **76**, 261–272.
- 18 M. Gigli, N. Lotti, M. Gazzano, L. Finelli and A. Munari, *React. Funct. Polym.*, 2012, **72**, 303–310.
- 19 M. Gigli, N. Lotti, M. Vercellino, L. Visai and A. Munari, *Mater. Sci. Eng., C*, 2014, **34**, 86–97.
- 20 M. Fabbri, M. Gigli, R. Gamberini, N. Lotti, M. Gazzano, B. Rimini and A. Munari, *Polym. Degrad. Stab.*, 2014, **108**, 223–231.
- 21 M. Mochizuki and M. Hiram, *Polym. Adv. Technol.*, 1997, **8**, 203–209.
- 22 H. C. Anderson, H. H. Hsu, P. Raval, P. R. Reynold, D. J. Gurley, M. X. Aguilera, L. S. Davis and P. E. Moylan, *Cells Mater.*, 1998, **8**, 89–98.
- 23 H. C. Anderson, H. H. Hsu, P. Raval, T. R. Hunt, J. R. Schwappach, D. C. Morris and D. J. Schneider, *Clin. Orthop. Relat. Res.*, 1995, **313**, 129–134.
- 24 H. C. Anderson, P. R. Reynolds, H. H. Hsu, L. Missana, K. Masuhara, P. E. Moylan and H. I. Roach, *J. Bone Miner. Metab.*, 2002, **20**, 73–82.
- 25 E. M. Czekanska, M. J. Stoddart, R. G. Richards and J. S. Hayes, *Eur. Cells Mater.*, 2012, **24**, 1–17.
- 26 H.-I. Chang and Y. Wang, in *Regenerative Medicine and Tissue Engineering - Cells and Biomaterials*, ed. D. Eberli, Intech, London, UK, 2011, vol. 27.
- 27 J. Lee, M. J. Cuddihy and N. A. Kotov, *Tissue Eng., Part B*, 2008, **14**, 61–86.
- 28 C. C. Lin and S. J. Fu, *Mater. Sci. Eng., C*, 2016, **58**, 254–263.
- 29 M. N. Andalib, J. S. Lee, L. Ha, Y. Dzenis and J. Y. Lim, *Biochem. Biophys. Res. Commun.*, 2016, **473**, 920–925.
- 30 M. J. Biggs and M. J. Dalby, *Proc. Inst. Mech. Eng., Part H*, 2010, **224**, 1441–1453.

- 31 M. D. Schofer, A. Veltum, C. Theisen, F. Chen, S. Agarwal, S. Fuchs-Winkelmann and J. R. Paletta, *J. Mater. Sci. Mater. Med.*, 2011, **22**, 1753–1762.
- 32 A. A. Khalili and M. R. Ahmad, *Int. J. Mol. Sci.*, 2015, **16**, 18149–18184.
- 33 S. Chakrabarti, M. Hinczewski and D. Thirumalai, *PNAS*, 2014, **111**, 9048–9053.
- 34 A. I. Alford, K. M. Kozloff and K. D. Hankenson, *Int. J. Biochem. Cell Biol.*, 2015, **65**, 20–31.
- 35 N. Ribeiro, S. R. Sousa and F. J. Monteiro, *J. Colloid Interface Sci.*, 2010, **351**, 398–406.
- 36 E. M. Rosset and A. D. Bradshaw, *Matrix Biol.*, 2016, **52–54**, 78–87.
- 37 F. Kahles, H. M. Findeisen and D. Bruemmer, *Mol. Metab.*, 2014, **3**, 384–393.
- 38 M. W. Stacey, J. Grubbs, A. Asmar, J. Pryor, H. Elsayed-Ali, W. Cao, A. Beskok, D. Dutta, D. A. Darby, A. Fecteau, A. Werner and R. E. Kelly Jr., *Connect. Tissue Res.*, 2012, **53**, 415–421.
- 39 J. Wei and G. Karsenty, *Curr. Osteoporos. Rep.*, 2015, **13**, 180–185.
- 40 M. Soccio, N. Lotti, M. Gigli, L. Finelli, M. Gazzano and A. Munari, *Polym. Int.*, 2012, **61**, 1163–1169.
- 41 M. Soccio, N. Lotti, L. Finelli, M. Gazzano and A. Munari, *Eur. Polym. J.*, 2008, **44**, 1722–1732.
- 42 T. Myata and T. Masuko, *Polymer*, 1998, **39**, 1399–1404.
- 43 R. Rezakhaniha, A. Agianniotis, J. T. C. Schrauwen, A. Griffa, D. Sage, C. V. C. Bouten, F. N. van de Vosse, M. Unser and N. Stergiopoulos, *Biomech. Model. Mechanobiol.*, 2012, **11**, 461–473.
- 44 C. Ayres, G. L. Bowlin, S. C. Henderson, L. Taylor, J. Shultz, J. Alexander, T. A. Telemeco and D. G. Simpson, *Biomaterials*, 2006, **27**, 5524–5534.
- 45 E. Saino, V. Maliardi, E. Quartarone, L. Fassina, L. Benedetti, M. G. C. De Angelis, P. Mustarelli, A. Facchini and L. Visai, *Tissue Eng., Part A*, 2010, **16**, 995–1008.
- 46 M. Van Engeland, L. J. W. Nieland, F. C. S. Ramaekers, B. Schutte and C. P. M. Reutelingsperger, *Cytometry*, 1998, **31**, 1–9.
- 47 G. Risi, N. Bloise, D. Merli, A. Icaro-Cornaglia, A. Profumo, M. Fagnoni, E. Quartarone, M. Imbriani and L. Visai, *RSC Adv.*, 2014, **4**, 18683–18693.
- 48 D. Prè, G. Ceccarelli, G. Gastaldi, A. Asti, E. Saino, L. Visai, F. Benazzo, M. G. Cusella De Angelis and G. Magenes, *Bone*, 2011, **49**, 295–303.
- 49 G. Ceccarelli, N. Bloise, M. Mantelli, G. Gastaldi, L. Fassina, M. G. De Angelis, D. Ferrari, M. Imbriani and L. Visai, *BioRes. Open Access*, 2013, **2**, 283–294.
- 50 N. Bloise, G. Ceccarelli, P. Minzioni, M. Vercellino, L. Benedetti, M. G. De Angelis, M. Imbriani and L. Visai, *J. Biomed. Opt.*, 2013, **18**, 128006.
- 51 E. Saino, S. Grandi, E. Quartarone, V. Maliardi, D. Galli, N. Bloise, L. Fassina, M. G. De Angelis, P. Mustarelli, M. Imbriani and L. Visai, *Eur. Cells Mater.*, 2011, **21**, 59–72.